Physics of Fluids

RESEARCH ARTICLE | MAY 03 2023

Non-equilibrium flow of van der Waals fluids in nano-channels

Shan Baochao (单保超); Ju Long (居隆); Su Wei (苏微); ... et. al

Physics of Fluids 35, 052004 (2023)
https://doi.org/10.1063/5.0148857

Physics of Fluids ARTICLE scitation.org/journal/phf

Non-equilibrium flow of van der Waals fluids in nano-channels

Cite as: Phys. Fluids **35**, 052004 (2023); doi: 10.1063/5.0148857
Submitted: 2 March 2023 · Accepted: 17 April 2023 ·
Published Online: 3 May 2023

Baochao Shan (单保超),[1] Long Ju (居隆),[2] Wei Su (苏微),[3,4] Zhaoli Guo (郭照立),[5,a)] and Yonghao Zhang (张勇豪)[6,a)]

AFFILIATIONS

[1]School of Engineering, University of Edinburgh, Edinburgh EH9 3FB, United Kingdom
[2]Computational Transport Phenomena Laboratory, Division of Physical Science and Engineering, King Abdullah University of Science and Technology, Thuwal 23955-6900, Saudi Arabia
[3]Division of Emerging Interdisciplinary Areas, The Hong Kong University of Science and Technology, Clear Water Bay, Hong Kong, China
[4]Department of Mathematics, The Hong Kong University of Science and Technology, Clear Water Bay, Hong Kong, China
[5]Institute of Interdisciplinary Research for Mathematics and Applied Science, Huazhong University of Science and Technology, Wuhan 430074, China
[6]State Key Laboratory of High-Temperature Gas Dynamics, Institute of Mechanics, Chinese Academy of Sciences, Beijing 100190, China

[a)]**Authors to whom correspondence should be addressed:** zlguo@hust.edu.cn and yonghao.zhang@imech.ac.cn

ABSTRACT

The Enskog–Vlasov equation provides a consistent description of the microscopic molecular interactions for real fluids based on the kinetic and mean-field theories. The fluid flows in nano-channels are investigated by the Bhatnagar–Gross–Krook (BGK) type Enskog–Vlasov model, which simplifies the complicated Enskog–Vlasov collision operator and enables large-scale engineering design simulations. The density distributions of real fluids are found to exhibit inhomogeneities across the nano-channel, particularly at large densities, as a direct consequence of the inhomogeneous force distributions caused by the real fluid effects including the fluid molecules' volume exclusion and the long-range molecular attraction. In contrast to the Navier–Stokes equation with the slip boundary condition, which fails to describe nano-scale flows due to the coexistence of confinement, non-equilibrium, and real fluid effects, the Enskog–Vlasov–BGK model is found to capture these effects accurately as confirmed by the corresponding molecular dynamics simulations for low and moderate fluid densities.

I. INTRODUCTION

Although significant progress has been achieved in fluid mechanics, it remains a research challenge to model real fluid flows at the nanoscale due to a plethora of underlying factors,[1,2] which involve the fluid molecules' volume exclusion and the long-range attraction between molecules. At the macroscopic level, fluid flows can be described by the conventional continuum models, such as the Navier–Stokes (NS) equations based on the mass, momentum, and energy conservations.[3] In such models, the microscopic dynamics of fluid molecules (such as the attractive and repulsive forces) are reflected by the transport coefficients, i.e., viscosity and thermal conductivity. The NS equations become invalid for non-equilibrium or strongly inhomogeneous (i.e., gas properties vary appreciably over a molecule size) fluid flows,[4] which are frequently encountered at the nanoscale where the surface confinement effect plays a non-negligible role.[5–7] While the density oscillation across the channel can be captured by the generalized hydrodynamic model,[8] the non-equilibrium effect is better to be studied by gas kinetic theory.[9]

The Boltzmann equation has been widely adopted to capture the non-equilibrium effect of dilute gas flows based on the assumption that the gas molecule size (σ) is negligibly smaller than the gas mean free path (λ), i.e., gas molecules are point-like with no finite spatial expansion,[10–12] as shown in Fig. 1(a). This assumption is appropriate for gas flows at relatively low pressures, such as aeronautics and astronautics,[13,14] micro-electromechanical systems,[15–17] and vacuum technology.[18,19] The degree of the non-equilibrium can be quantified by

the Knudsen number (Kn), which is defined as the ratio of the gas mean free path to the characteristic flow length(H), i.e.,

$$\mathrm{Kn} = \frac{\lambda}{H}. \tag{1}$$

Based on the value of Kn, dilute gas flows can be divided into four flow regimes, i.e., continuum flow ($\mathrm{Kn} < 0.001$), slip flow ($0.001 < \mathrm{Kn} < 0.1$), transition flow ($0.1 < \mathrm{Kn} < 10$), and free molecular flow ($\mathrm{Kn} > 10$).[20] In recent decades, the majority of studies have been focusing on the non-equilibrium flow of dilute gases. However, with advancements in high-pressure shock tubes[21] and injection systems,[22] shale gas development,[23–26] and geological storage of carbon dioxide,[27–30] the real fluid effect due to non-negligible molecular attraction has become important. This has sparked great interest in the study of dense gas dynamics.[31–33] While molecular dynamics (MD) simulations can be used to investigate the dynamics of both dilute and dense gases, their application to practical problems is limited by their prohibitive computational cost.[33] As kinetic methods are more computationally efficient, we will focus on the kinetic description of dense gas dynamics. As the gas pressure dramatically increases, the size of a gas molecule becomes comparable with both the gas mean free path and the characteristic length of flow field, as shown in Fig. 1(b), consequently the real fluid and confinement effects come into play.[12,34] The finite size of fluid molecules (i.e., the fluid volume exclusion effect) is taken into account in the Enskog theory for dense fluids,[35,36] which is more accurate than the Boltzmann equation to describe non-equilibrium flows of dense fluids.[10,31]

The finite size of fluid molecules plays its role in several folds. First, the collision frequency between fluid molecules is changed. On the one hand, the volume of fluid molecules reduces the available space for free streaming; hence, the collision frequency is increased. On the other hand, the shielding of one molecule by another reduces the collision frequency.[36] The total change in the collision frequency is a combined effect of both factors, which can be quantified by the radial distribution function (χ).[37] Second, when the fluid volume exclusion is not negligible, the momentum and energy of fluids are transferred not only during molecular motions but also through non-localized collisions between molecules.[38,39] This modifies the transport coefficients of dense fluids.[40] The dense fluid effect caused by the change in collision frequency and non-localized collisions can be characterized by the reduced density (η) defined as the fraction of volume occupied by fluid molecules, i.e.,

$$\eta = \frac{n\pi\sigma^3}{6}, \tag{2}$$

where n is the fluid number density and σ is the molecular diameter. Bird[41] pointed out that the dense fluid effect becomes non-negligible when $\delta/\sigma < 7$ with $\delta = n^{-1/3}$ being the average distance between molecules, which approximately corresponds to the reduced density $\eta > 0.0015$. Third, the center of fluid molecules can never reach the physical boundary if the fluid molecule size is considered, as shown in Fig. 1(b). As a consequence, the effective flow domain is reduced by one molecular diameter;[10] this becomes particularly important in determining flow properties at the nanoscale since the reduction of the effective flow domain quantified by $1/C$ becomes comparable to the total flow path size, with C being the confinement factor, i.e.,

$$C = \frac{H}{\sigma}. \tag{3}$$

The confinement effect arises when the confinement factor becomes small. It is noted that the confinement effect should also include the surface potential accounting for fluid adsorption near the solid surface,[34,42–44] which is not considered in this study, since our main research focus is on the real fluid effect from fluid–fluid molecular interactions.

The original Enskog theory for dense fluids was first extended from the Boltzmann equation,[45] where the finite size of fluid molecules is included through the modification of collision frequency and the non-localized binary collisions. In this respect, the original Enskog theory is only applicable to hard-sphere fluids without considering the long-range attraction among fluid molecules. However, the importance of molecular attraction has been demonstrated in the van der Waals theory,[46,47] which can be modeled as a local point force by the mean-field theory. By adding a Vlasov approximation term[47] to the Enskog equation, the Enskog–Vlasov (EV) equation[48,49] can be obtained, wherein both the fluid volume exclusion and the long-range attraction among molecules[50] are considered. It is noted here that the real fluid effect arises from both the fluid volume exclusion and the long-range attraction, while the dense fluid effect arises only from the volume exclusion.

The EV equation provides a unified description of both liquid and vapor phases and has been effectively solved using direct simulation Monte Carlo (DSMC).[48,51] However, large-scale engineering applications of the EV equation are restricted by its formidable computational cost in evaluating the collision operator, which is in a complex integral form.[52,53] As a particle-based method, DSMC is subjected to significant statistical noise when the flow velocity is much smaller than the molecular thermal velocity.[54] Furthermore, the computational cost of DSMC increases proportionally with the number of simulated molecules, making it more expensive for dense fluids.[55] Therefore, simplified EV model equations are proposed using the

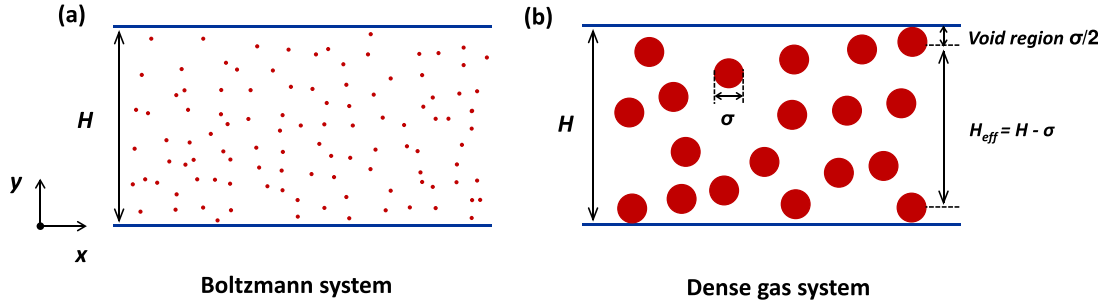

FIG. 1. Schematic of confined flow systems based on (a) the dilute gas assumption and (b) dense fluid assumption.

relaxation time approach.[31,42,56,57] In this paper, the surface-confined flows of real fluids will be analyzed by the Enskog–Vlasov–BGK (EV-BGK) model,[42,56,57] whose accuracy will be validated by MD simulations. The rest of the paper is organized as follows: Sec. II briefly describes the EV-BGK model and its related properties; the MD setup details are also given in this section. In Sec. III, the non-equilibrium flow of real fluids is investigated by the EV-BGK model at different densities, confinement, temperature, and fluid molecular attraction conditions. Section IV summarizes the main findings of the present study.

II. PROBLEM SETUP AND SIMULATION TECHNIQUES

The isothermal force-driven Poiseuille flows are investigated as the test cases. As shown in Fig. 1, both dilute and dense fluids are confined between two parallelled plates with a separation of H, and the channel averaged density is maintained at n_{avg} for all the cases as

$$n_{avg} = \frac{1}{H}\int_0^H n(y)\,\mathrm{d}y. \tag{4}$$

Meanwhile, the system temperature is chosen to be $T = 273\,\mathrm{K}$, and the external force in the flow direction is chosen according to the flow configurations to ensure that all the flows are in the linear flow regime.

A. The Enskog–Vlasov–BGK model

The EV equation can be derived from the BBGKY hierarchy to describe a hard-sphere fluid under an attractive force field,[47] which can be written as

$$\frac{\partial f}{\partial t} + \boldsymbol{\xi}\cdot\nabla_r f + \boldsymbol{a}\nabla_\xi f = \Omega_{hs} + \Omega_{mf}, \tag{5}$$

where $f(\boldsymbol{r}, \boldsymbol{\xi}, t)$ is the velocity distribution function with $\boldsymbol{r}$ being the position, $\boldsymbol{\xi}$ being the molecular velocity, and t being the time; $\boldsymbol{a}$ is the acceleration rate, which is related to the external force through $\boldsymbol{a} = \boldsymbol{G}/m$ with m being the mass of a fluid molecule; and Ω_{hs} is the hard-sphere collision operator, which can be expressed as

$$\begin{aligned}\Omega_{hs} = \sigma^2 \int\int \Big[&\chi\left(\boldsymbol{r} + \frac{1}{2}\sigma\boldsymbol{k}\right) f(\boldsymbol{r}, \boldsymbol{\xi}') f_1(\boldsymbol{r} + \sigma\boldsymbol{k}, \boldsymbol{\xi}_1') \\ &- \chi\left(\boldsymbol{r} - \frac{1}{2}\sigma\boldsymbol{k}\right) f(\boldsymbol{r}, \boldsymbol{\xi}) f_1(\boldsymbol{r} - \sigma\boldsymbol{k}, \boldsymbol{\xi}_1)\Big]\boldsymbol{g}\cdot\boldsymbol{k}\,\mathrm{d}\boldsymbol{k}\,\mathrm{d}\boldsymbol{\xi}_1,\end{aligned} \tag{6}$$

where $\boldsymbol{k}$ is a unit vector that assigns the relative position of two molecules at the time of their impact; $\boldsymbol{g} = \boldsymbol{\xi} - \boldsymbol{\xi}_1$ is the relative velocity of two colliding molecules, with $\boldsymbol{\xi}$ and $\boldsymbol{\xi}_1$ being the molecular velocities before collisions; $\boldsymbol{\xi}'$ and $\boldsymbol{\xi}_1'$ are the post-collision molecular velocities; and Ω_{mf} is the mean-field force term to describe the fluid attraction among molecules, which can be expressed as

$$\Omega_{mf} = \frac{1}{m}\nabla\left[\int_{|\boldsymbol{r}'|>\sigma} n(\boldsymbol{r}+\boldsymbol{r}')\phi_{att}(|\boldsymbol{r}'|)\,\mathrm{d}\boldsymbol{r}'\right]\cdot\nabla_\xi f, \tag{7}$$

where ϕ_{att} is the attractive potential between two molecules, i.e.,

$$\phi_{att} = \begin{cases} 0, & |\boldsymbol{r}'| < \sigma, \\ -4\epsilon\left(\dfrac{\sigma}{r'}\right)^6, & |\boldsymbol{r}'| \geq \sigma. \end{cases} \tag{8}$$

Equations (5)–(7) formulate the final form of the EV equation. However, the hard-sphere collision operator Ω_{hs} is complicated and its evaluation is time-consuming, which restricts its engineering applications. Relaxation-time models have been proposed to simplify the collision operator.[31,42,56,57] Following these procedures, the Bhatnagar–Gross–Krook (BGK) model[58] is employed to represent the hard-core collision process, while the fluid volume exclusion is considered by an excess collision term. Therefore, the EV-BGK model can be written as[42,59]

$$\frac{\partial f}{\partial t} + \boldsymbol{\xi}\cdot\nabla_r f + \boldsymbol{a}\nabla_\xi f = \Omega_0 + \Omega_{ex} + \Omega_{mf}, \tag{9}$$

where Ω_0 and Ω_{ex} are the BGK collision operator and the excess collision operator, respectively, which can be expressed as

$$\begin{aligned}\Omega_0 &= -\frac{1}{\tau}(f - f^{eq}), \\ \Omega_{ex} &= -V_0 f^{eq}(\boldsymbol{\xi} - \boldsymbol{u})\cdot(2\boldsymbol{A}\chi + \boldsymbol{B}n).\end{aligned} \tag{10}$$

It is noted that Ω_0 and Ω_{ex} account for the hard-core collision and the fluid volume exclusion effect on collisions, respectively, from a physical perspective. The Maxwellian local equilibrium distribution function f^{eq} is defined as

$$f^{eq} = n\left(\frac{m}{2\pi k_B T}\right)^{\frac{3}{2}}\exp\left[-\frac{m(\boldsymbol{\xi}-\boldsymbol{u})^2}{2k_B T}\right]. \tag{11}$$

The radial distribution function χ can be obtained from the Carnahan and Starling equation of state[60] as

$$\chi = \frac{1 - 0.5\eta}{(1-\eta)^3}, \tag{12}$$

where the reduced density η is evaluated at the local average density $\bar{n} = \int_{|\boldsymbol{r}'|<\sigma/2}\omega(\boldsymbol{r}')n(\boldsymbol{r}+\boldsymbol{r}')\,\mathrm{d}\boldsymbol{r}'$,[61] so Eq. (2) transforms into

$$\eta = 0.25\bar{n}V_0 = \frac{\bar{n}\pi\sigma^3}{6}, \tag{13}$$

where $V_0 = 2\pi\sigma^3/3$ is the second-order virial coefficient in the virial expansion of the equation of state. In Eq. (10), $\boldsymbol{A}$ and $\boldsymbol{B}$, as proposed by Guo *et al.*[42] for inhomogeneous fluids, can be expressed as

$$\begin{aligned}\boldsymbol{A}(\boldsymbol{r}) &= \frac{120}{\pi\sigma^5}\int_{|\boldsymbol{r}'|<\sigma/2}\boldsymbol{r}'\bar{n}(\boldsymbol{r}+\boldsymbol{r}')\,\mathrm{d}\boldsymbol{r}', \\ \boldsymbol{B}(\boldsymbol{r}) &= \frac{120}{\pi\sigma^5}\int_{|\boldsymbol{r}'|<\sigma/2}\boldsymbol{r}'\chi(\bar{n})\,\mathrm{d}\boldsymbol{r}'.\end{aligned} \tag{14}$$

When fluid density varies slowly across the channel, the local average density is approximately equal to the fluid density, so that $\bar{n} \approx n$, and $\boldsymbol{A}$ and $\boldsymbol{B}$ reduce to

$$\boldsymbol{A} \approx \nabla n, \quad \boldsymbol{B} \approx \nabla\chi. \tag{15}$$

On the continuum level, the EV equation (5) and the EV-BGK model (9) correspond to the van der Waals-type equation of state,[8,49,59] which can be written as

$$p = nk_BT(1 + nV_0\chi) + p^{att}, \tag{16}$$

where p^{att} is the attractive contribution to the equilibrium pressure. Therefore, the EV-type equations describe real fluid dynamics with both the repulsive and attractive forces among fluid molecules. In comparison, it is the hard-sphere fluids that the original Enskog theory describes where the molecular attraction is ignored. In this paper, the real fluid flows will be investigated by the EV-BGK model, and the importance of long-range attraction will be elucidated by comparing the dynamics of real and hard-sphere fluids.

B. Solution of the kinetic model

The EV-BGK model (9) is solved by the discrete unified gas kinetic scheme[62–64] together with the fully diffuse boundary condition[65] expressed as

$$f(\boldsymbol{r}_w, \boldsymbol{\xi}_i) = f^{eq}(n_w, \boldsymbol{u}_w, \boldsymbol{\xi}_i), \quad \boldsymbol{\xi}_i \cdot \boldsymbol{n} > 0, \tag{17}$$

where n_w is the fluid density at the wall determined by the condition that no particles go through the boundary, $\boldsymbol{u}_w$ is the velocity of a moving wall, and $\boldsymbol{n}$ is the inward unit vector normal to the wall. For the Poiseuille flow, $\boldsymbol{u}_w = 0$ since both plates are stationary.

The relaxation time τ relates to the fluid viscosity[31] through

$$\tau = \frac{\mu}{p}, \tag{18}$$

where $p = nk_{BT}$ is the homogeneous fluid pressure[66] and μ is the fluid viscosity determined by the Enskog theory[36] for dense fluids as

$$\mu = \mu_0 Y, \tag{19}$$

with

$$\mu_0 = 1.016\frac{5}{16\sigma^2}\sqrt{\frac{mk_BT}{\pi}} \tag{20}$$

being the fluid viscosity at atmospheric pressure, and

$$Y = \bar{n}V_0\left[\frac{1}{\bar{n}V_0\chi(\bar{n})} + 0.8 + 0.7614\bar{n}V_0\chi(\bar{n})\right] \tag{21}$$

being a correction function for fluid viscosity at high densities.

The macroscopic density and velocity can be determined by taking moments of the velocity distribution function as

$$\begin{aligned} n &= \int f \, \mathrm{d}\xi, \\ n\boldsymbol{u} &= \int \xi f \, \mathrm{d}\xi. \end{aligned} \tag{22}$$

C. MD setup for surface-confined flows

MD simulations are conducted to provide benchmark data to assess the performance of the EV-BGK model (9). All simulations are run using the large-scale atomic/molecular massively parallel simulator (LAMMPS). To be consistent with the setup in the kinetic model, the number of fluid molecules N in MD is controlled by the average density n_{avg} via

$$N = n_{avg} L_x L_z H, \tag{23}$$

where L_x and L_z are the lengths of the physical domain in MD simulations in the x and z directions, respectively, as shown in Fig. 2.

The interactions among fluid molecules are described by the Lennard–Jones (LJ) potential

$$\phi_{LJ} = 4\epsilon\left[\left(\frac{\sigma}{r'}\right)^{12} - \left(\frac{\sigma}{r'}\right)^{6}\right], \quad r' < r_c, \tag{24}$$

where ϵ and σ are the energy and length parameters and r_c is the cutoff distance, which is chosen to be $r_c = 1.2$ nm in this study.

In the MD simulations, an external force G_x is imposed on all the fluid particles along the channel, which drives the fluid to flow in the x direction. Periodic boundary conditions are employed in the x and z directions, while the fully diffuse boundary condition is applied to the

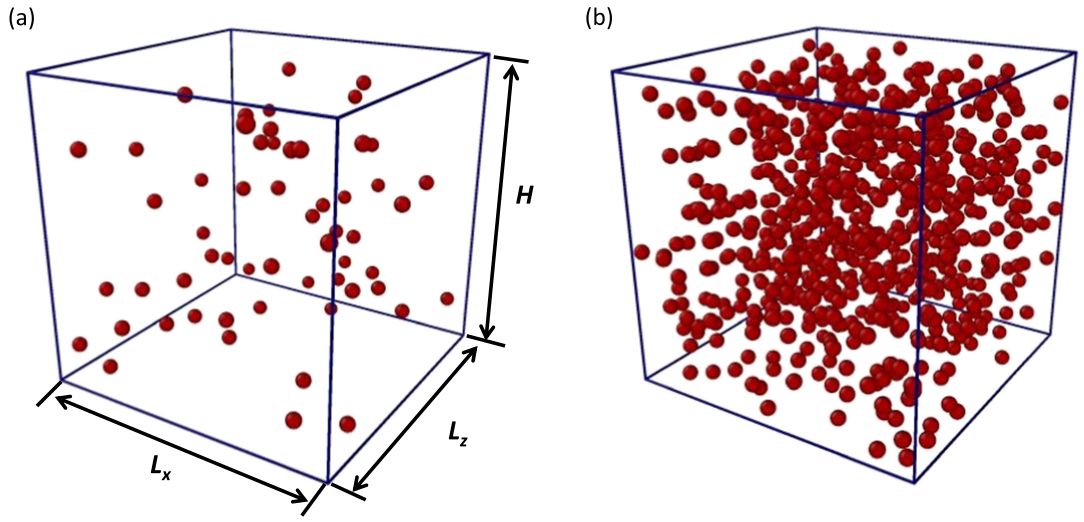

FIG. 2. Schematic of the physical model in MD simulations. (a) $\rho = 30$ kg/m^3 and (b)$\rho = 350$ kg/m^3.

TABLE I. The chosen parameters for the tested cases.

Cases	ρ, kg/^{3}	H, nm	T, K	G_x, kcal/(mol ·Å)	Kn	η	H/σ
1	21.2	2	273	0.001	3.001	0.0066	5.88
2	117.3	2	273	0.0005	0.5006	0.0365	5.88
3	695.0	2	273	0.0005	0.0501	0.2163	5.88
4	8.53	5	273	0.001	3.0020	0.0027	14.69
5	49.5	5	273	0.0005	0.5010	0.0154	14.69
6	216.0	5	273	0.0003	0.1002	0.0672	14.69
7	376.0	5	273	0.0003	0.0501	0.1170	14.69
8	450.0	5	273	0.0003	0.0392	0.1400	14.69
9	695.0	5	273	0.0003	0.0200	0.2163	14.69
10	216.0	50	273	0.000 03	0.0100	0.0672	146.9

channel walls. The system temperature is maintained at $T = 273$ K through the Nosé–Hoover thermostat. The time step is set to be 1 fs.

III. RESULTS AND DISCUSSION

In this section, density and velocity distributions of surface-confined flows predicted by the EV-BGK model are compared to the MD simulation data. The density inhomogeneity arising from the real fluid effect is revealed, which is a direct result of the inhomogeneous total force distribution among fluid molecules across the channel. The effects of fluid molecular attraction and system temperature on nanoscale flows are also analyzed.

A. Density and velocity distributions of nanoscale flows

Fluid density and velocity distributions under different density and confinement conditions are investigated in this part, with corresponding parameters summarized in Table I. The external force G_x is chosen to ensure that flows are in the linear regime. The Knudsen number can be calculated as

$$\mathrm{Kn} = \frac{1}{\sqrt{2}n\pi\sigma^2\chi H} = \frac{1}{6\sqrt{2}\eta\chi C}, \tag{25}$$

which relates to the dense fluid effect (η) and the confinement effect (C) at the same time.

The density and velocity distributions across a 2-nm nanochannel at $\rho_{avg} = 21.2$, 117.3, and 695.0 kg/m^3 are shown in Figs. 3–5, respectively. The fluid density ρ_{avg} relates to the fluid number density n_{avg} through $\rho_{avg} = mn_{avg}$. The fluid volume exclusion plays an important role in fluid flows under tight confinements and leads to a void region near each wall marked by the shadow in Fig. 3. There is tiny density inhomogeneity when fluid density is as small as 21.2 kg/m^3, see Fig. 3(a). This density inhomogeneity becomes discernible when fluid density increases to 117.3 kg/m^3 as shown in Fig. 4(a) and is more significant at $\rho_{avg} = 695.0$ kg/m^3 as shown in Fig. 5(a). More obvious density inhomogeneities indicate a stronger real fluid effect at higher fluid densities. Meanwhile, it is worth noting that fluid–solid interactions are not considered in this paper, so the density inhomogeneity is a direct consequence of the real fluid effect, so the density peak near the wall is not caused by fluid adsorption, see Fig. 5(a) for example.

The velocity distributions predicted by the NS equation with the second-order slip boundary condition are also given as a reference of the conventional continuum theory in each case. The slip boundary condition is written as

$$u_s - u_w = \pm C_1\lambda\left(\frac{\partial u}{\partial n}\right)_s - C_2\lambda^2\left(\frac{\partial^2 u}{\partial n^2}\right)_s, \tag{26}$$

where u_s and $(\partial u/\partial n)_s$ represent the velocity and velocity gradient at the boundary; C_1 and C_2 are the first- and second-order slip

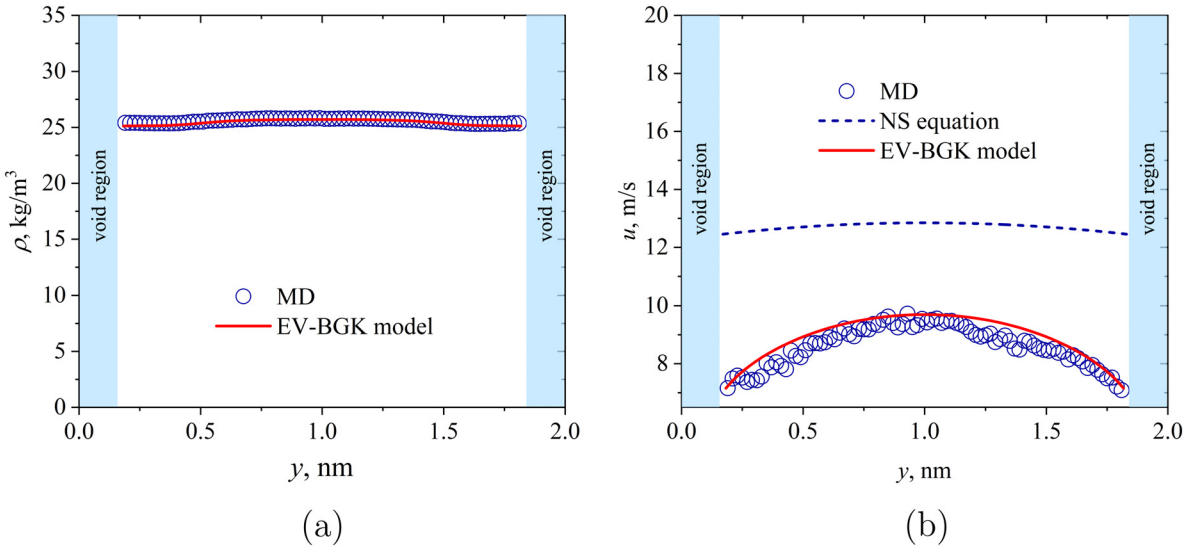

FIG. 3. Density (a) and velocity (b) distributions of fluid flows in a 2-nm nanochannel with the averaged density $\rho_{avg} = 21.2$ kg/m^3. The corresponding Knudsen number is Kn = 3.001.

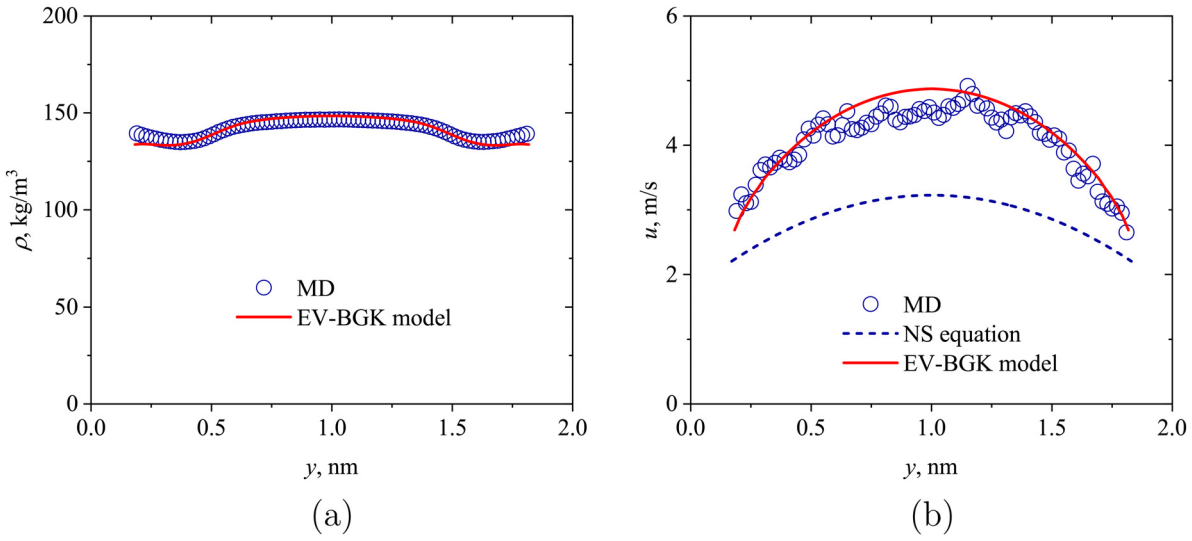

FIG. 4. Density (a) and velocity (b) distributions of fluid flows in a 2-nm nanochannel with the averaged density $\rho_{avg} = 117.3$ kg/m^3. The corresponding Knudsen number is Kn = 0.5006.

coefficients, respectively, which are chosen to be $C_1 = 1.0$ and $C_2 = 0.5$ as derived from the linearized Boltzmann equation.[36] Although the molecule size is not considered in the conventional continuum theory, we technically use the effective channel size $H_{eff} = H - \sigma$ as an input in the NS equations for comparisons. Since the interactions among fluid molecules are reflected by the transport coefficients (e.g., viscosity and thermal conductivity) at the continuum level, the NS equations become invalid for nano-scale flows where fluid density inhomogeneities arise and the non-equilibrium effect becomes significant. Overall, the velocity distributions agree well with each other at different densities between the EV-BGK model and MD simulations, see Figs. 3(b), 4(b), and 5(b), indicating the capability of the EV-BGK model in capturing the real fluid and non-equilibrium effects.

As shown in Fig. 5, the simulated density and velocity profiles predicted by the EV-BGK model partly deviate from the MD data at $\rho = 695$ kg/m^3. This is because the EV-BGK model is based on the binary collision assumption, which may not be true for flows at high densities where multiple collisions may become non-negligible.

As the channel size increases to 5 nm, the overall performance of the EV-BGK model is similar to fluid flows in 2-nm channels, see Figs. 6–11. At small densities (i.e., larger Kn), the NS equation overestimates

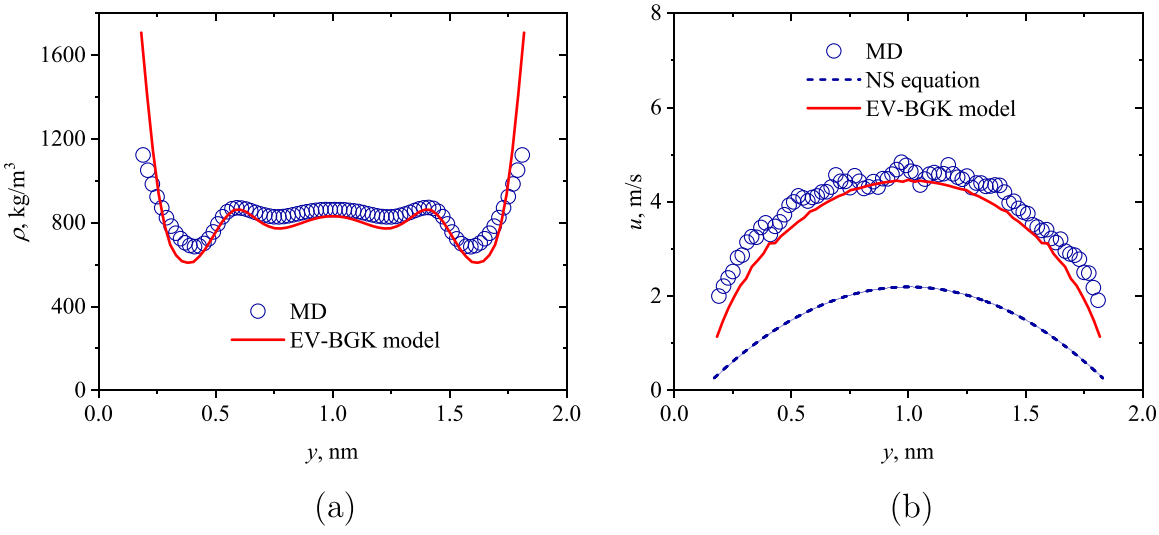

FIG. 5. Density (a) and velocity (b) distributions of fluid flows in a 2-nm nanochannel with the averaged density $\rho_{avg} = 695.0$ kg/m^3. The corresponding Knudsen number is Kn = 0.0501.

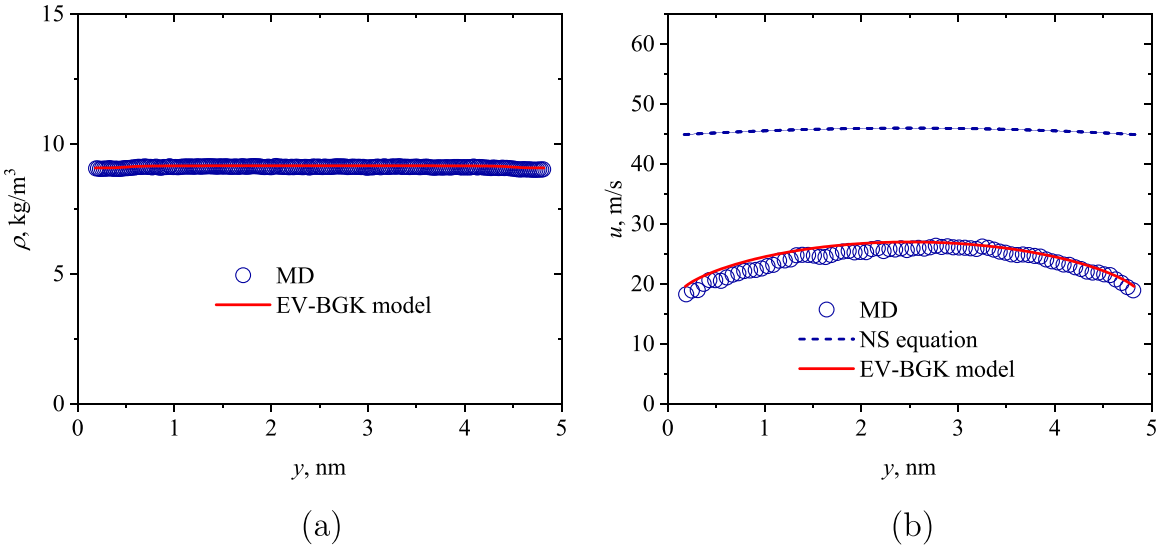

FIG. 6. Density (a) and velocity (b) distributions of fluid flows in a 5-nm nanochannel with the averaged density $\rho_{avg} = 8.53$ kg/m^3. The corresponding Knudsen number is Kn = 3.002.

the velocity profiles, see Fig. 6(b). When the density increases (i.e., Kn decreases), the non-equilibrium effect becomes weaker, so the NS predictions approach to the EV-BGK model and MD simulations. Within the density range considered in this paper (8.53–695.0 kg/m^3), the EV-BGK model gives satisfactory results compared to the MD simulations.

To better clarify the confinement effect, we extend the channel size to 50 nm, with the density and velocity profiles shown in Fig. 12. In this case, the void region near the wall is barely discernible, indicating that the fluid volume exclusion has a negligible effect on the effective channel size. Although there is a slight non-equilibrium effect (Kn = 0.01), the NS predictions of velocities are very close to the EV-BGK and MD results. We can infer that as the channel size further increases, the MD (microscopic), EV-BGK model (mesoscopic), and NS equation (macroscopic) will produce the same results as the non-equilibrium, real fluid, and confinement effects become negligible.

The EV-BGK model is computationally more efficient as solved by the discrete unified gas kinetic scheme than MD simulations. For example, to simulate a gas flow in a 5-nm nano-channel with the

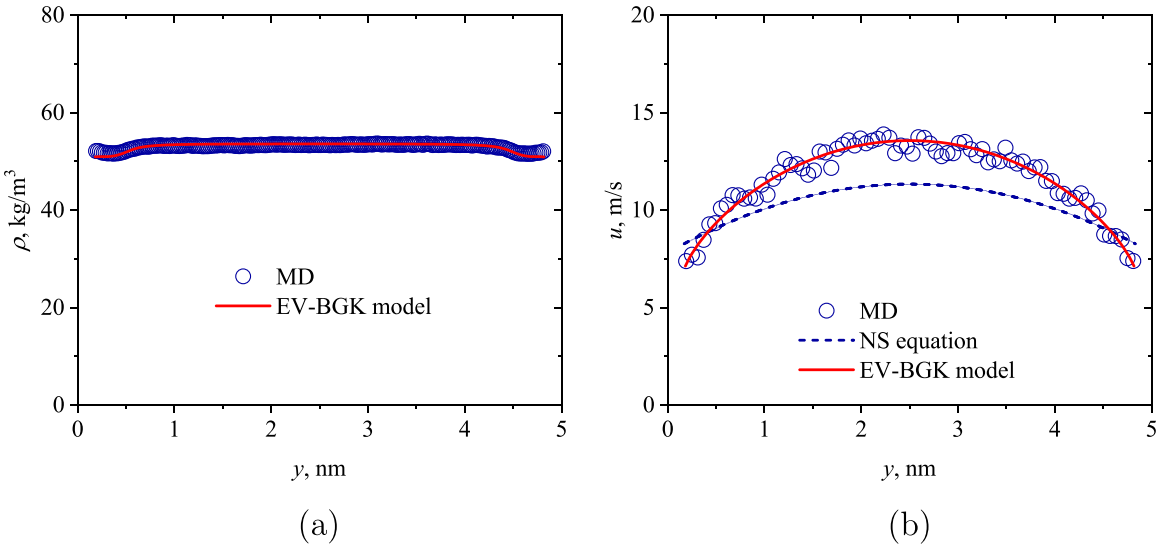

FIG. 7. Density (a) and velocity (b) distributions of fluid flows in a 5-nm nanochannel with the averaged density $\rho_{avg} = 49.5$ kg/m^3. The corresponding Knudsen number is Kn = 0.5010.

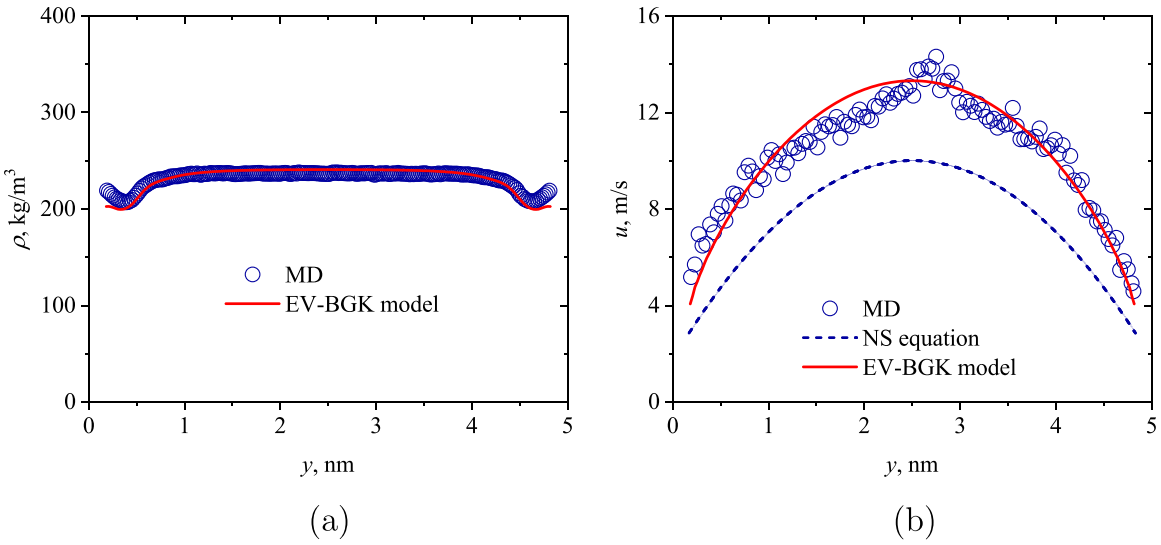

FIG. 8. Density (a) and velocity (b) distributions of fluid flows in a 5-nm nanochannel with the averaged density $\rho_{avg} = 216.0$ kg/m^3. The corresponding Knudsen number is Kn = 0.1002.

pore average density of 216 kg/m^3, the external force of 0.0003 kcal/(mol Å), and the system temperature of 273 K, significantly shorter computational time of 37 s is required for the EV-BGK model using 1 Central Processing Unit (CPU) core while approximately 20 min is needed for MD simulation using 128 message passing interface (MPI) cores. Additionally, MD simulations suffer from considerable statistical noise for low-speed flows, necessitating additional running steps and resulting in heavier computational burdens. Low-speed flows are widespread in natural and engineering applications, such as shale gas production[67] and nanoscale evaporating flows,[51] whereas our kinetic model offers exceptional computational efficiency in these scenarios. It is also worth noting that pressure boundary conditions for the inlet and outlet can be conveniently set up in the kinetic framework using extrapolation or non-equilibrium extrapolation schemes. However, generating a pressure difference between the inlet and outlet in MD simulations requires additional computational domains,[68] leading to a significant increase in computational cost. Proper pressure boundary conditions are particularly important for inhomogeneous flows, as pressure-driven and force-driven flows can exhibit differences in the flowfield features.[68]

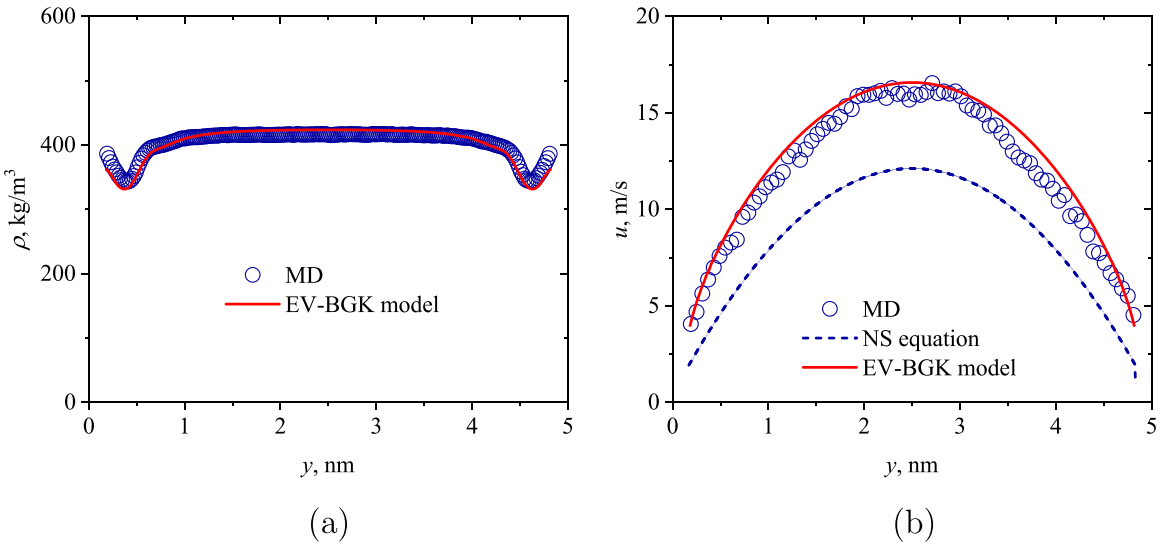

FIG. 9. Density (a) and velocity (b) distributions of fluid flows in a 5-nm nanochannel with the averaged density $\rho_{avg} = 376.0$ kg/m^3. The corresponding Knudsen number is Kn = 0.0501.

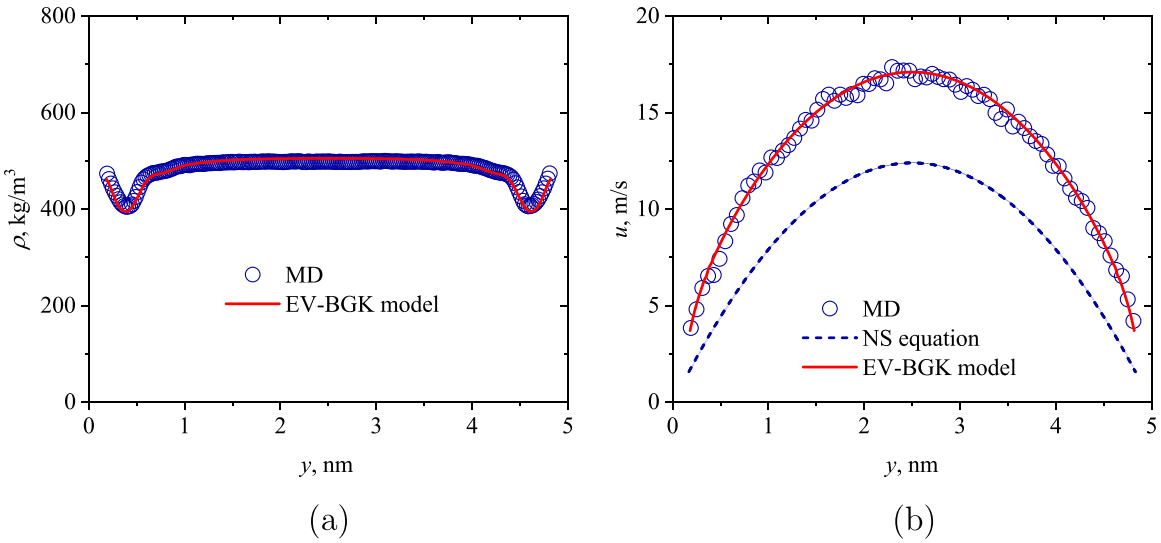

FIG. 10. Density (a) and velocity (b) distributions of fluid flows in a 5-nm nanochannel with the averaged density $\rho_{avg} = 450.0$ kg/m^3. The corresponding Knudsen number is Kn = 0.0392.

B. Force distribution across the channel

The real fluid effect manifests itself as the repulsive and attractive forces between fluid molecules on the microscopic level. According to the mean-field and Enskog theories, the attractive and repulsive forces can be approximated by Eqs. (7) and (10), respectively. The distributions of both attractive and repulsive as well as their total forces of case 9, see Table I, are shown in Fig. 13. Due to the inhomogeneous intermolecular interactions between fluid molecules, the values of these forces change more violently near the wall than in the bulk region, implying the complexities of fluids in the boundary layer. This also directly leads to a more inhomogeneous density distribution adjacent to the wall compared to the bulk region. The total force, which is the microscopic origin of the real fluid effect, is also compared with the MD data in Fig. 13(b), demonstrating accuracy of the Enskog and mean-field theories in modeling real fluids.

The total force distribution across the channel directly leads to density inhomogeneities, particularly at high densities. According to the relationship between the force ($\boldsymbol{G}$) and the potential (ϕ), i.e.,

$$\boldsymbol{G} = -\frac{\partial \phi}{\partial \boldsymbol{r}}, \tag{27}$$

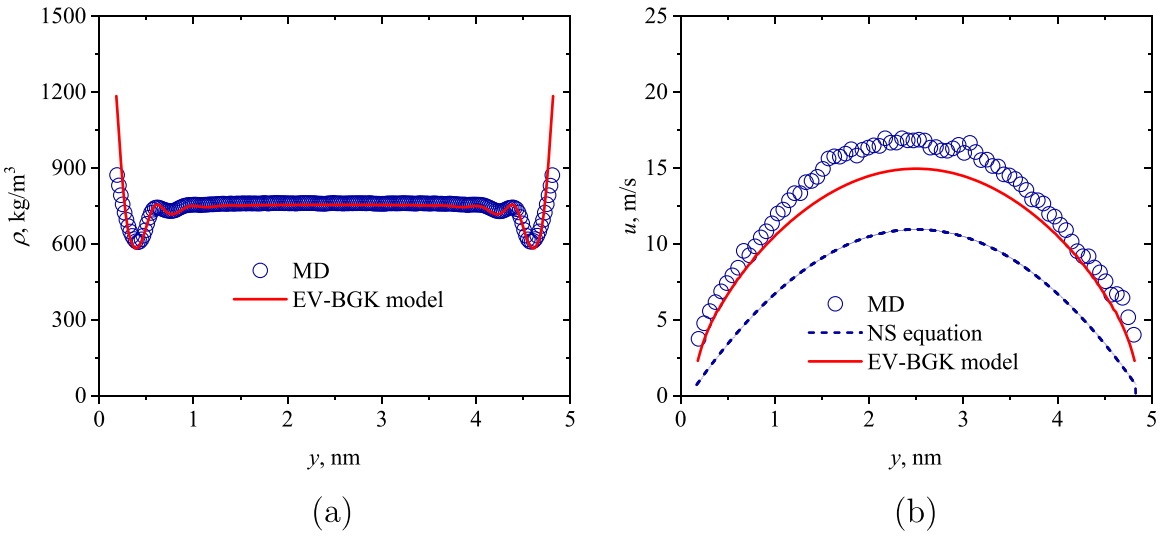

FIG. 11. Density (a) and velocity (b) distributions of fluid flows in a 5-nm nanochannel with the averaged density $\rho_{avg} = 695.0$ kg/m^3. The corresponding Knudsen number is Kn = 0.02.

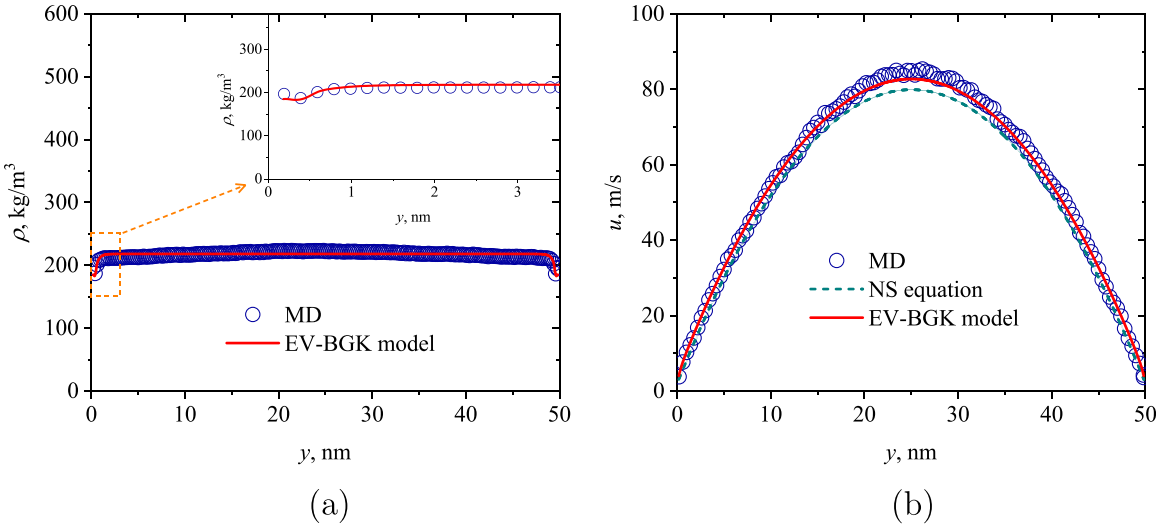

FIG. 12. Density (a) and velocity (b) distributions of fluid flows in a 50-nm nanochannel with the averaged density $\rho_{avg} = 216.0$ kg/m^3. The insert is an enlargement of the density distribution near the wall. The corresponding Knudsen number is Kn = 0.01.

the intersections between the total force profile and the zero force line correspond to the potential wells, which result in density peaks and valleys, as shown in Fig. 14. This further illustrates that the strong real fluid effect may lead to the density inhomogeneity, which is different from the fluid adsorption caused by fluid–solid interactions.[69–71]

C. Effect of fluid molecular attraction

Real fluid molecules attract each other in the long-range, which is modeled by the attractive potential in Eq. (8) and coupled into the kinetic model through the mean-field force term Ω_{mf} in Eq. (7). The attraction strength is characterized by the energy parameter ϵ. In this part, the energy parameter ϵ is changed to $0.8\epsilon_{Ar}$ and $1.1\epsilon_{Ar}$ to represent weak and strong attraction cases, respectively, where ϵ_{Ar} is the energy parameter of Argon used in this study. If the mean-field force term Ω_{mf} is ignored, the EV-BGK model reduces to the Engkog–BGK model, which describes the dynamics of hard-sphere fluids, i.e., no attractive forces among fluid molecules. The fluid attraction works as an internal pressure to pull fluid molecules inward into the flow domain, so the fluid density adjacent to the wall becomes smaller as

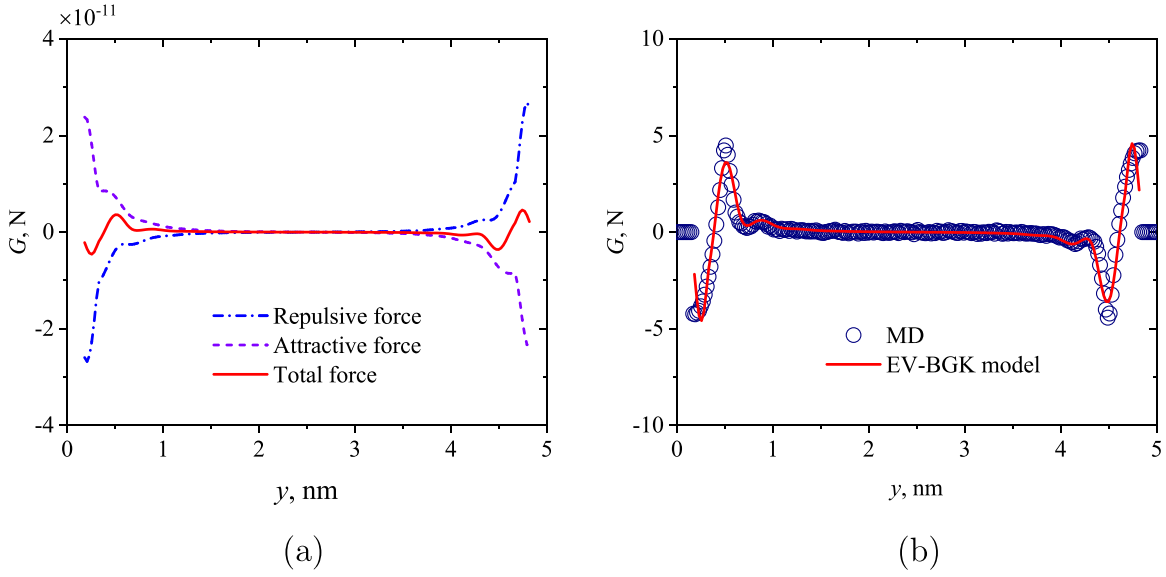

FIG. 13. The distribution of attractive, repulsive, and total forces among fluid molecules. (a) EV-BGK model results and (b) a comparison of the total forces calculated from the EV-BGK model and MD.

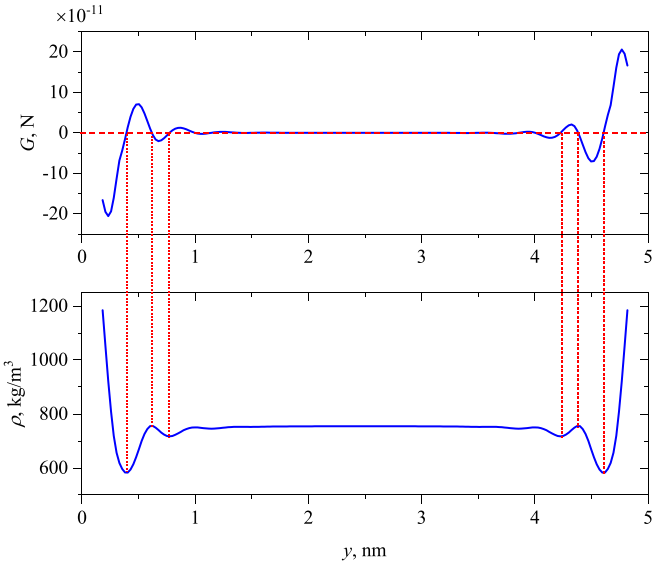

FIG. 14. The correlation between the total force and density distributions.

fluid attraction becomes stronger. As shown in Fig. 15, the hard-sphere fluid density near the wall is the largest as no attraction exists. This straightforward observation can be justified by the equation of state (16), wherein, if the attractive force field (8) is chosen, the attractive contribution to the equilibrium pressure can be written as

$$p^{att} = -\frac{16\pi}{3}\sigma^3\epsilon n^2. \tag{28}$$

Clearly, the fluid molecular attraction works as an internal negative pressure in fluid equilibrium phase properties. Corresponding to densities at different molecular attractions, the slip velocity increases as fluid molecular attraction becomes stronger. This is because a stronger fluid attraction leads to a smaller fluid density near the wall and thus less efficient momentum exchange between the fluids and the wall.

D. Effect of system temperature

The temperature affects density and velocity profiles similar to fluid molecular attractions. At high temperatures, fluid molecules possess more kinetic energy to overcome the attraction from surrounding molecules, hence exhibiting like a weaker attraction among fluid molecules. Consequently, the boundary layer density increases, and the slip velocity decreases with the temperature, as shown in Fig. 16. Again, the EV-BGK model produces satisfactory results compared to the MD data.

E. Slip velocity of real fluids

The EV-BGK model reduces to the Boltzmann-BGK model when the fluid volume exclusion term Ω_{ex} and the fluid attraction term Ω_{mf} are omitted, which describes the dynamics of ideal fluids. The slip velocities of ideal, hard-sphere, and real fluids are shown in Fig. 17, which increase with the Kn in all the cases, i.e., a stronger non-equilibrium effect at a larger Kn. The slip velocities of hard-sphere and real fluids tend to be the same as the Kn increases, indicating that fluid attraction plays a negligible role at large Kn. With the increase in the channel size, real fluid dynamics approaches to ideal ones as the confinement and real fluid effects become less important.

To evaluate the role of confinement and real fluid effects, the variation of non-dimensional slip velocity with Kn is measured as shown in Fig. 17(b), where the slip velocity is normalized by $u_r = \sqrt{2k_BT/m}$. The non-dimensional slip velocity of the ideal gas coincides with flows at different channel sizes (2 and 5 nm), indicating that ideal gas flows are characterized solely by Kn. The non-dimensional slip velocity is different for hard-sphere and real fluids at different confinements, indicating that both confinement and real fluid effects play their roles. This is

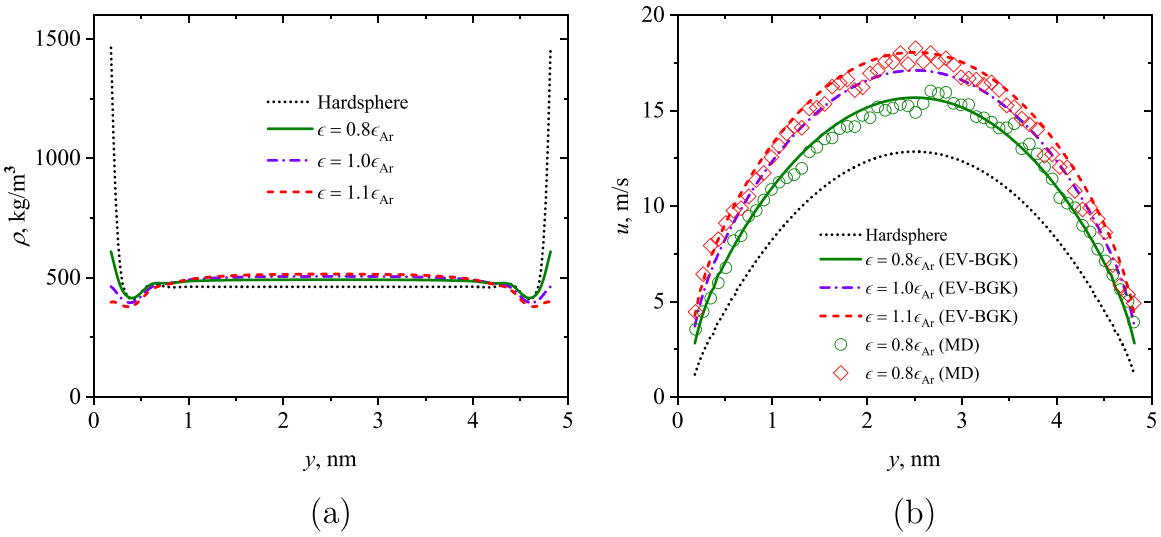

FIG. 15. Density (a) and velocity (b) distributions of fluid flows at different fluid attraction strengths.

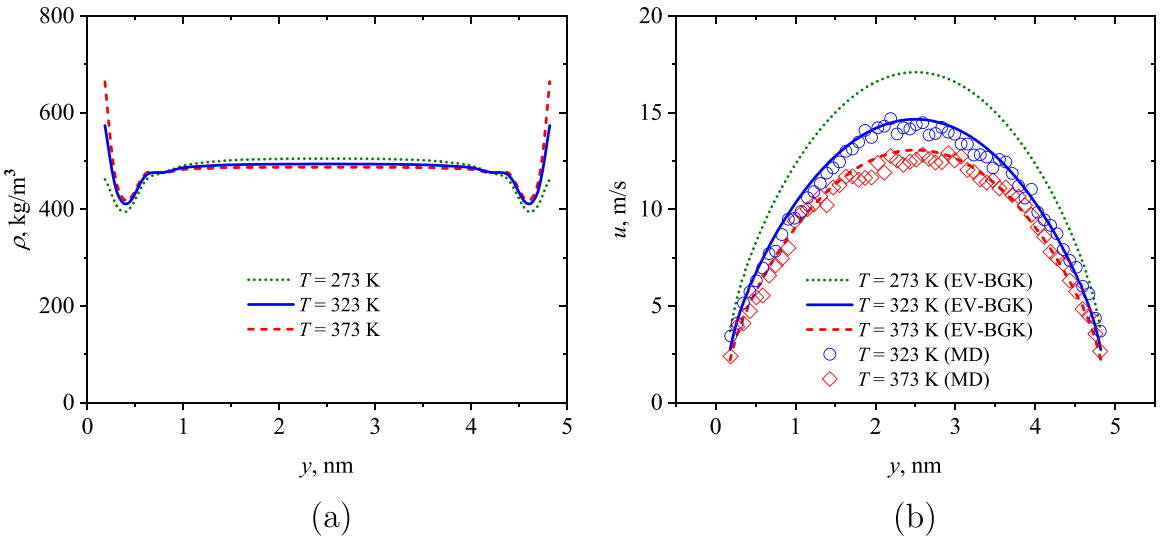

FIG. 16. Density (a) and velocity (b) distributions of fluid flows at different temperatures.

similar to the disappearance of the Knudsen minimum for dense gases under confinements observed in previous studies.[10,12] Therefore, fluid flows under confinements are controlled by both confinement and real fluid effects.

IV. CONCLUSIONS

In this paper, the force-driven Poiseuille flows of real fluids at the nanoscale are investigated by the EV-BGK model at different non-equilibrium and confinement conditions. The simulated results are validated by the MD simulation data. The effects of fluid attraction and system temperature on fluid flows are also analyzed. From this study, the following conclusions can be drawn:

(1) The EV-BGK model produces satisfactory density and velocity profiles for real fluid flows within the density range from 8.5 to 695.0 kg/m^3, which shows its capability in capturing the real fluid effect at large densities and the non-equilibrium effect at large Kn.
(2) Due to the force imbalance caused by the real fluid effect, fluid density exhibits inhomogeneities in nano-scale flows, which are more significantly close to the surface as a consequence of more inhomogeneous intermolecular interactions between fluid molecules.
(3) The fluid attraction pulls fluid molecules inward into the flow domain and makes the density distribution less inhomogeneous compared to the hard-sphere cases. Therefore, the fluid density

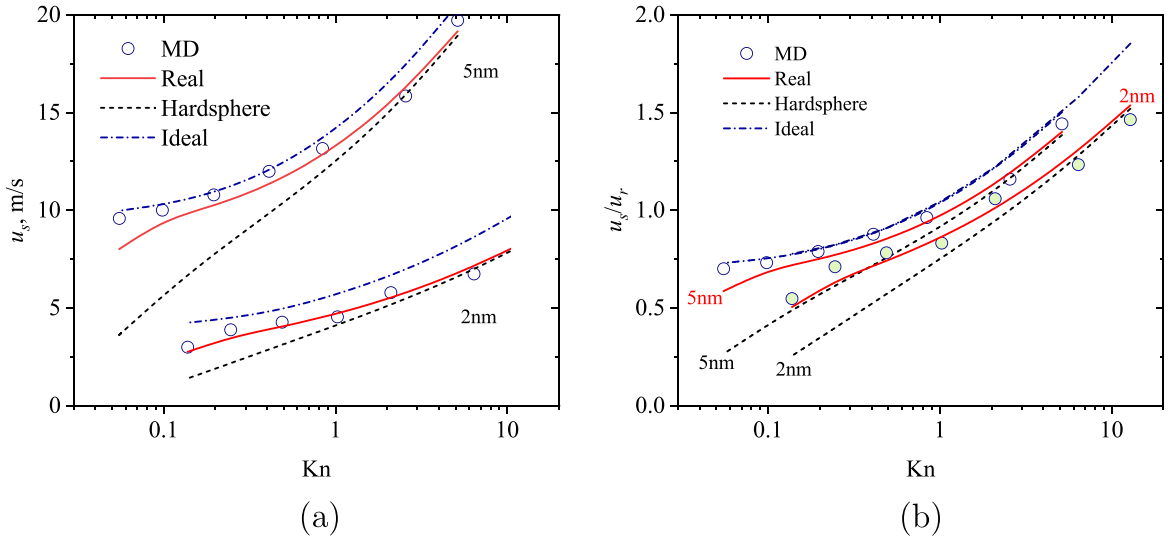

FIG. 17. Variation of slip velocity (a) and non-dimensional slip velocity (b) with Kn.

in boundary layers will be overestimated, and the slip velocity will be underestimated for real fluids if the long-range attraction is ignored.

Due to its high accuracy and computational efficiency, there is significant interest in extending the EV-BGK model to more complex gas systems, including polyatomic and reacting gases, as well as complex geometries. In addition, this model has the potential to investigate fundamental problems, such as liquid–vapor phase transition[51] and two-phase flows in porous media.[72] However, it should be noted that, like other BGK-type models, the EV-BGK model produces a fixed Prandtl number of unity, which restricts its application to isothermal flows. Therefore, more sophisticated models should be developed to handle non-isothermal cases where heat fluxes are significant.

ACKNOWLEDGMENTS

This paper was dedicated to Dr. Peng Wang, an eminent young scholar and a genuine friend to all of us. He brought many excellent ideas to the research community, including but not limited to the heat transfer of three-dimensional turbulent natural convection flow where he established a novel correlation between the Nusselt number and the Rayleigh number up to 10^{10}, the rarefied gas flows in all flow regimes based on the DUGKS where he revealed that the damping force and heat flow can be controlled by changing the aspect ratio of the geometry and the oscillating frequency of the moving part in micro-devices, and the multiscale modelling where he widened the applicable scope of traditional CFD by incorporating the non-equilibrium effect into the constitutive equation and boundary condition. His work on the kinetic model of the Enskog equation paves the way for the study of non-equilibrium dynamics of dense gases, which is key to understanding the transport of dense gases. This paper is in memory of him for his contribution to this research line.

This work was supported by the UK's Engineering and Physical Sciences Research Council under Grant No. EP/R041938/1 and the National Natural Science Foundation of China under Grant Nos. 51836003 and 12002130. Supercomputing time on ARCHER is provided by the "UK Consortium on Mesoscale Engineering Sciences (UKCOMES)" under the UK Engineering and Physical Sciences Research Council Grant No. EP/R029598/1. This work made use of computational support by CoSeC, the Computational Science Centre for Research Communities, through UKCOMES.

AUTHOR DECLARATIONS

Conflict of Interest

The authors have no conflicts to disclose.

Author Contributions

Baochao Shan: Conceptualization (equal); Data curation (equal); Formal analysis (equal); Investigation (equal); Methodology (equal); Software (equal); Validation (equal); Visualization (equal); Writing – original draft (equal). **Long Ju:** Conceptualization (equal); Investigation (equal); Methodology (equal). **Wei Su:** Conceptualization (equal); Investigation (equal); Methodology (equal). **Zhaoli Guo:** Project administration (equal); Supervision (equal); Writing – review & editing (equal). **Yonghao Zhang:** Project administration (equal); Supervision (equal); Writing – review & editing (equal).

DATA AVAILABILITY

The data that support the findings of this study are available from the corresponding authors upon reasonable request.

REFERENCES

[1]T. F. Viscondi, A. Grigolo, I. L. Caldas, and J. R. Meneghini, "Slippery-sticky transition of interfacial fluid slip," Phys. Fluids **33**, 062012 (2021).
[2]B. Shan, L. Ju, Z. Guo, and Y. Zhang, "Investigation of shale gas flows under confinement using a self-consistent multiscale approach," Adv. Geo-Energy Res. **6**, 537 (2022).
[3]K. P. Travis, B. Todd, and D. J. Evans, "Departure from Navier-Stokes hydrodynamics in confined liquids," Phys. Rev. E **55**, 4288 (1997).
[4]I. Bitsanis, T. Vanderlick, M. Tirrell, and H. Davis, "A tractable molecular theory of flow in strongly inhomogeneous fluids," J. Chem. Phys. **89**, 3152–3162 (1988).
[5]F. Wang, J. Qian, J. Fan, J. Li, H. Xu, and H. Wu, "Molecular transport under extreme confinement," Sci. China Phys., Mech. Astron. **65**, 264601 (2022).
[6]H. Yu, H. Xu, J. Xia, J. Fan, F. Wang, and H. Wu, "Nanoconfined transport characteristic of methane in organic shale nanopores: The applicability of the continuous model," Energy Fuels **34**, 9552–9562 (2020).
[7]Q. Sheng, L. Gibelli, J. Li, M. K. Borg, and Y. Zhang, "Dense gas flow simulations in ultra-tight confinement," Phys. Fluids **32**, 092003 (2020).
[8]Z. Guo, T. Zhao, and Y. Shi, "Generalized hydrodynamic model for fluid flows: From nanoscale to macroscale," Phys. Fluids **18**, 067107 (2006).
[9]W. Su, Q. Li, Y. Zhang, and L. Wu, "Temperature jump and Knudsen layer in rarefied molecular gas," Phys. Fluids **34**, 032010 (2022).
[10]L. Wu, H. Liu, J. M. Reese, and Y. Zhang, "Non-equilibrium dynamics of dense gas under tight confinement," J. Fluid Mech. **794**, 252–266 (2016).
[11]J. Mathiaud and L. Mieussens, "Mesoscopic Boltzmann model equations for thermally perfect gases," Phys. Fluids **33**, 127112 (2021).
[12]C. Corral-Casas, J. Li, M. K. Borg, and L. Gibelli, "Knudsen minimum disappearance in molecular-confined flows," J. Fluid Mech. **945**, A28 (2022).
[13]R. Martinez-Val and E. Perez, "Aeronautics and astronautics: Recent progress and future trends," Proc. Inst. Mech. Eng., Part C **223**, 2767–2820 (2009).
[14]W. Su, L. Zhu, P. Wang, Y. Zhang, and L. Wu, "Can we find steady-state solutions to multiscale rarefied gas flows within dozens of iterations?," J. Comput. Phys. **407**, 109245 (2020).
[15]O. Ejtehadi, E. Roohi, and J. A. Esfahani, "Investigation of basic molecular gas structural effects on hydrodynamics and thermal behaviors of rarefied shear driven micro/nano flow using DSMC," Int. Commun. Heat Mass Transfer **39**, 439–448 (2012).
[16]S. E. Lyshevski, *Nano-and Micro-Electromechanical Systems: Fundamentals of Nano-and Microengineering* (CRC Press, 2018).
[17]Y. Zhang, P. Wang, and Z. Guo, "Oscillatory couette flow of rarefied binary gas mixtures," Phys. Fluids **33**, 027102 (2021).
[18]S. Varoutis, D. Valougeorgis, O. Sazhin, and F. Sharipov, "Rarefied gas flow through short tubes into vacuum," J. Vac. Sci. Technol. A **26**, 228–238 (2008).
[19]N. Bykov and V. Zakharov, "Binary gas mixture outflow into vacuum through an orifice," Phys. Fluids **32**, 067109 (2020).
[20]Y. Zhang, L. Zhu, P. Wang, and Z. Guo, "Discrete unified gas kinetic scheme for flows of binary gas mixture based on the Mccormack model," Phys. Fluids **31**, 017101 (2019).
[21]E. L. Petersen and R. K. Hanson, "Nonideal effects behind reflected shock waves in a high-pressure shock tube," Shock Waves **10**, 405–420 (2001).
[22]R. N. Dahms and J. C. Oefelein, "Non-equilibrium gas–liquid interface dynamics in high-pressure liquid injection systems," Proc. Combust. Inst. **35**, 1587–1594 (2015).
[23]Y. Wu, P. Tahmasebi, C. Lin, M. J. Munawar, and V. Cnudde, "Effects of micropores on geometric, topological and transport properties of pore systems for low-permeability porous media," J. Hydrol. **575**, 327–342 (2019).

[24]J. Cai, T. Jin, J. Kou, S. Zou, J. Xiao, and Q. Meng, "Lucas–washburn equation-based modeling of capillary-driven flow in porous systems," Langmuir **37**, 1623–1636 (2021).
[25]W. Shen, X. Li, T. Ma, J. Cai, X. Lu, and S. Zhou, "High-pressure methane adsorption behavior on deep shales: Experiments and modeling," Phys. Fluids **33**, 063103 (2021).
[26]S. Luo, C. Ding, H. Cheng, B. Zhang, Y. Zhao, and L. Liu, "Estimated ultimate recovery prediction of fractured horizontal wells in tight oil reservoirs based on deep neural networks," Adv. Geo-Energy Res. **6**, 111 (2022).
[27]L. Ju, B. Shan, P. Liu, and Z. Guo, "Pore-scale study of miscible density-driven mixing flow in porous media," Phys. Fluids **33**, 034113 (2021).
[28]X. Zhu, L. Chen, S. Wang, Q. Feng, and W. Tao, "Pore-scale study of three-phase displacement in porous media," Phys. Fluids **34**, 043320 (2022).
[29]Y. Wang, C. Vuik, and H. Hajibeygi, "Co_2 storage in deep saline aquifers: Impacts of fractures on hydrodynamic trapping," Int. J. Greenhouse Gas Control **113**, 103552 (2022).
[30]L. Ju, B. Shan, and S. Wang, "Pore-scale study on miscible thermal displacing process in porous media using lattice Boltzmann method," Phys. Fluids **35**, 023109 (2023).
[31]P. Wang, L. Wu, M. T. Ho, J. Li, Z.-H. Li, and Y. Zhang, "The kinetic Shakhov–Enskog model for non-equilibrium flow of dense gases," J. Fluid Mech. **883**, A48 (2020).
[32]W. Su, L. Gibelli, J. Li, M. K. Borg, and Y. Zhang, "Kinetic modeling of non-equilibrium flow of hard-sphere dense gases," Phys. Rev. Fluids **8**, 013401 (2023).
[33]S. Busuioc, "Quadrature-based lattice Boltzmann model for non-equilibrium dense gas flows," Phys. Fluids **35**, 016112 (2023).
[34]B. Shan, R. Wang, Z. Guo, and P. Wang, "Contribution quantification of nano-scale gas transport in shale based on strongly inhomogeneous kinetic model," Energy **228**, 120545 (2021).
[35]D. M. Gass, "Enskog theory for a rigid disk fluid," J. Chem. Phys. **54**, 1898–1902 (1971).
[36]S. Chapman and T. G. Cowling, *The Mathematical Theory of Non-Uniform Gases: An Account of the Kinetic Theory of Viscosity, Thermal Conduction and Diffusion in Gases* (Cambridge University Press, 1990).
[37]H. Van Beijeren and M. H. Ernst, "The modified Enskog equation," Physica **68**, 437–456 (1973).
[38]D. K. Hoffman and C. Curtiss, "Kinetic theory of dense gases. III. The generalized Enskog equation," Phys. Fluids **7**, 1887–1897 (1964).
[39]H. Hanley, R. McCarty, and E. Cohen, "Analysis of the transport coefficients for simple dense fluid: Application of the modified Enskog theory," Physica **60**, 322–356 (1972).
[40]J. Dymond, "Corrected Enskog theory and the transport coefficients of liquids," J. Chem. Phys. **60**, 969–973 (1974).
[41]G. A. Bird, *Molecular Gas Dynamics and the Direct Simulation of Gas Flows* (Clarendon Press, Oxford, 1994).
[42]Z. Guo, T. Zhao, and Y. Shi, "Simple kinetic model for fluid flows in the nanometer scale," Phys. Rev. E **71**, 035301 (2005).
[43]T. Zhang, F. Javadpour, X. Li, K. Wu, J. Li, and Y. Yin, "Mesoscopic method to study water flow in nanochannels with different wettability," Phys. Rev. E **102**, 013306 (2020).
[44]B. Shan, P. Wang, R. Wang, Y. Zhang, and Z. Guo, "Molecular kinetic modelling of nanoscale slip flow using a continuum approach," J. Fluid Mech. **939**, A9 (2022).
[45]D. Enskog, "The numerical calculation of phenomena in fairly dense gases," Ark. Mat., Astron. Fys **16**, 1–60 (1921).
[46]J. Vera and J. Prausnitz, "Generalized van der Waals theory for dense fluids," Chem. Eng. J. **3**, 1–13 (1972).
[47]X. He and G. D. Doolen, "Thermodynamic foundations of kinetic theory and lattice Boltzmann models for multiphase flows," J. Stat. Phys. **107**, 309–328 (2002).
[48]A. Frezzotti, L. Gibelli, and S. Lorenzani, "Mean field kinetic theory description of evaporation of a fluid into vacuum," Phys. Fluids **17**, 012102 (2005).
[49]M. Sadr and M. H. Gorji, "Treatment of long-range interactions arising in the Enskog–Vlasov description of dense fluids," J. Comput. Phys. **378**, 129–142 (2019).
[50]J. Karkheck and G. Stell, "Kinetic mean-field theories," J. Chem. Phys. **75**, 1475–1487 (1981).
[51]A. Frezzotti, P. Barbante, and L. Gibelli, "Direct simulation Monte Carlo applications to liquid-vapor flows," Phys. Fluids **31**, 062103 (2019).
[52]E. Benilov and M. Benilov, "Energy conservation and h theorem for the Enskog-Vlasov equation," Phys. Rev. E **97**, 062115 (2018).
[53]H. Struchtrup and A. Frezzotti, "Twenty-six moment equations for the Enskog–Vlasov equation," J. Fluid Mech. **940**, A40 (2022).
[54]L. Wu, Y. Zhang, and J. M. Reese, "Fast spectral solution of the generalized Enskog equation for dense gases," J. Comput. Phys. **303**, 66–79 (2015).
[55]E. Roohi and M. Darbandi, "Recommendations on performance of parallel DSMC algorithm in solving subsonic nanoflows," Appl. Math. Modell. **36**, 2314–2321 (2012).
[56]L. Luo, "Unified theory of lattice Boltzmann models for nonideal gases," Phys. Rev. Lett. **81**, 1618 (1998).
[57]X. He, X. Shan, and G. D. Doolen, "Discrete Boltzmann equation model for nonideal gases," Phys. Rev. E **57**, R13 (1998).
[58]P. L. Bhatnagar, E. P. Gross, and M. Krook, "A model for collision processes in gases. I. Small amplitude processes in charged and neutral one-component systems," Phys. Rev. **94**, 511 (1954).
[59]B. Shan, S. Chen, Z. Guo, and P. Wang, "Pore-scale study of non-ideal gas dynamics under tight confinement considering rarefaction, denseness and molecular interactions," J. Nat. Gas Sci. Eng. **90**, 103916 (2021).
[60]N. F. Carnahan and K. E. Starling, "Equation of state for nonattracting rigid spheres," J. Chem. Phys. **51**, 635–636 (1969).
[61]P. Tarazona, "Free-energy density functional for hard spheres," Phys. Rev. A **31**, 2672 (1985).
[62]Z. Guo, K. Xu, and R. Wang, "Discrete unified gas kinetic scheme for all Knudsen number flows: Low-speed isothermal case," Phys. Rev. E **88**, 033305 (2013).
[63]Z. Guo and K. Xu, "Progress of discrete unified gas-kinetic scheme for multi-scale flows," Adv. Aerodyn. **3**, 6 (2021).
[64]B. Shan, P. Wang, Y. Zhang, and Z. Guo, "Discrete unified gas kinetic scheme for all Knudsen number flows. IV. Strongly inhomogeneous fluids," Phys. Rev. E **101**, 043303 (2020).
[65]Y. Zhang, L. Zhu, R. Wang, and Z. Guo, "Discrete unified gas kinetic scheme for all Knudsen number flows. III. Binary gas mixtures of Maxwell molecules," Phys. Rev. E **97**, 053306 (2018).
[66]L. Ju, B. Shan, Z. Yang, and Z. Guo, "An exact non-equilibrium extrapolation scheme for pressure and velocity boundary conditions with large gradients in the lattice Boltzmann method," Comput. Fluids **231**, 105163 (2021).
[67]J. Cai, D. Lin, H. Singh, S. Zhou, Q. Meng, and Q. Zhang, "A simple permeability model for shale gas and key insights on relative importance of various transport mechanisms," Fuel **252**, 210–219 (2019).
[68]Q. Guan, B. Shan, R. Wang, G. Feng, and Z. Guo, "Evaluation of different particle-actuation modes in molecular dynamics and their impact on nanoscale flow behaviors," Phys. Fluids **34**, 072006 (2022).
[69]W. Shen, X. Li, A. Cihan, X. Lu, and X. Liu, "Experimental and numerical simulation of water adsorption and diffusion in shale gas reservoir rocks," Adv. Geo-Energy Res. **3**, 165–174 (2019).
[70]Y. Zhao, X. Liu, L. Zhang, and B. Shan, "A basic model of unconventional gas microscale flow based on the lattice Boltzmann method," Pet. Explor. Dev. **48**, 179–189 (2021).
[71]L. Zhang, C. Liu, Q. Li, S. Wang, S. Cai, and E. Huo, "Shale gas transport through the inorganic cylindrical and conical nanopores: A density gradient driven molecular dynamics," Int. J. Heat Mass Transfer **183**, 122126 (2022).
[72]Y. Wu, P. Tahmasebi, K. Liu, S. Fagbemi, C. Lin, S. An, and L. Ren, "Two-phase flow in heterogeneous porous media: A multiscale digital model approach," Int. J. Heat Mass Transfer **194**, 123080 (2022).